THE JOURNAL OF BIOLOGICAL CHEMISTRY VOL. 286, NO. 37, pp. 32123–32131, September 16, 2011

Ca^{2+} Binding Alters the Interdomain Flexibility between the Two Cytoplasmic Calcium-binding Domains in the Na^+/Ca^{2+} Exchanger*[S]

Received for publication, April 8, 2011, and in revised form, July 18, 2011 Published, JBC Papers in Press, July 21, 2011, DOI 10.1074/jbc.M111.249268

Roberto K. Salinas[‡§1], **Lei Bruschweiler-Li**[‡§], **Eric Johnson**[‡§2], **and Rafael Brüschweiler**[‡§3]

From the [‡]*Department of Chemistry and Biochemistry, Florida State University, Tallahassee, Florida 32306-4390 and the* [§]*National High Magnetic Field Laboratory, Florida State University, Tallahassee, Florida 32310*

The Na^+/Ca^{2+} exchanger (NCX) is a membrane protein, which catalyzes the counter transport of Na^+ and Ca^{2+} ions across the plasma membrane, playing a key role in the maintenance of the intracellular Ca^{2+} homeostasis in various cell types. NCX consists of a transmembrane part and a large intracellular loop. The activation of the NCX transport function requires the binding of Ca^{2+} to two tandem C2 domains, CBD1 and CBD2, which are an integral part of the exchanger's intracellular loop. Although high-resolution structures of individual CBD1 and CBD2 are available, their interdomain structure and dynamics and the atomic level mechanism of allosteric Ca^{2+}-regulation remains unknown. Here, we use solution NMR spectroscopy to study the interdomain dynamics of CBD12, a 32 kDa construct that contains both the CBD1 and CBD2 domains connected by a short linker. Analysis of NMR residual dipolar couplings shows that CBD12 assumes on average an elongated shape both in the absence and in the presence of Ca^{2+}. NMR ^{15}N relaxation data of the Apo state indicate that the two domains sample a wide range of relative arrangements on the nanosecond time scale. These arrangements comprise significantly non-linear interdomain orientations. Binding of Ca^{2+} to CBD1 significantly restricts the interdomain flexibility, stabilizing a more rigid elongated conformation. These findings suggest a molecular mechanism for the role of CBD12 in the function of NCX.

The Na^+/Ca^{2+} exchanger (NCX)[4] is a membrane protein that maintains intracellular Ca^{2+} homeostasis. The NCX is the primary Ca^{2+} extrusion mechanism in the heart and the brain (1–3). In addition to being substrates, Na^+ and Ca^{2+} also have regulatory functions: cytosolic Ca^{2+} acts as an allosteric activator, while intracellular Na^+ inhibits the exchanger. The latter process, called Na^+-dependent inactivation, can be reversed by the increase of intracellular Ca^{2+} (2, 3).

The mature canine NCX1 consists of two transmembrane regions, formed by 5 and 4 transmembrane segments (TM), separated by a large intracellular loop between TM5 and TM6 (2, 3). The intracellular loop contains two tandem calcium-binding domains (CBDs), CBD1 (residues 371–501) and CBD2 (residues 504–657 in the AD splice variant studied here) (4). The CBD domains share an immunoglobulin (Ig) fold, formed by two antiparallel β-sheets, which pack against each other forming a β-sandwich, and a large unstructured loop connecting strands F and G at the opposite side of the β-sandwich (4–8). CBD1 and CBD2 bind four and two Ca^{2+} ions, respectively (5, 6). The Ca^{2+}-binding sites lie at the tip of the β-sandwich. This topology is very similar to C2 domains, a class of Ca^{2+}-binding motifs that are ubiquitous in nature, and frequently involved in signal transduction and membrane traffic (9).

While the transmembrane regions of the exchanger conduct ion transport (3, 10), extensive electrophysiological data obtained with the wild type and mutant exchangers have implicated CBD1 and CBD2 in Ca^{2+} regulation (6, 11, 12). However, despite detailed structural and dynamics data obtained about the isolated CBD domains (4–6, 13–15), the mechanism by which the binding of regulatory Ca^{2+} modulates the exchanger activity is not understood. The binding of Ca^{2+} to the isolated CBDs was shown to restrict the motions of the Ca^{2+}-binding loops (13, 15). It is possible, however, that in the full-length NCX, interactions between CBD1 and CBD2 introduce new structural and dynamic effects that could be involved in allosteric Ca^{2+} regulation. Consistent with this hypothesis, stopped flow measurements of Ca^{2+} dissociation kinetics from a tandem construct, CBD12, which contains both the CBD1 and CBD2 domains connected by a short linker, showed that interdomain interactions modulate the Ca^{2+} dissociation rate at a specific Ca^{2+}-binding site in the CBD1 domain (16). SAXS (14) and FRET (17) measurements have recently demonstrated that binding of Ca^{2+} to CBD1 induces conformational changes in CBD12. Conformational changes in the cytoplasmic loop of full-length functional exchanger were also observed by FRET (17). However, the atomic details of such conformational changes remain unknown.

To understand at the atomic level how binding of Ca^{2+} to the cytoplasmic CBD domains is involved in allosteric Ca^{2+} regulation of the NCX, we have pursued studies of the solution

* This work was supported by Grant MCB-0918362 of the National Science Foundation.

The backbone resonance assignments were deposited in the Biological Magnetic Resonance Bank (BMRB) under the accession numbers 17721 and 17722.

[S] The on-line version of this article (available at http://www.jbc.org) contains supplemental Figs. S1–S4 and Table S1.

[1] Recipient of postdoctoral fellowship from the American Heart Association.

[2] Recipient of postdoctoral fellowship from the American Heart Association. Present address: Dept. of Chemistry and Physical Sciences, College of Mount St. Joseph, Cincinnati, OH 45233.

[3] To whom correspondence should be addressed: 95 Chieftan Way Rm. 118 DLC, Florida State University, Tallahassee, FL 32306-4390. Tel.: 850-644-1768; Fax: 850-644-8281; E-mail: bruschweiler@magnet.fsu.edu.

[4] The abbreviations used are: NCX, Na^+/Ca^{2+} exchanger; CBD, calcium-binding domain; RDC, residual dipolar coupling; CSP, chemical shift perturbation.

structure and dynamics of the tandem CBD12 construct by high-resolution NMR spectroscopy. Measurements of backbone ^{15}N relaxation, residual dipolar couplings (RDCs), and chemical shift perturbations indicate that the two CBDs are flexibly linked in the absence of Ca^{2+}. Binding of Ca^{2+} to CBD1 dramatically strengthens the dynamic coupling between the two domains by restricting the flexibility of the interdomain linker such that CBD1 and CBD2 move less freely with respect to each other. RDC analysis indicates that the overall molecular shape of CBD12 is largely elongated in the Apo and Ca^{2+}-bound states. Based on these findings it is postulated that changes in interdomain flexibility due to Ca^{2+} binding are part of the allosteric Ca^{2+} regulation mechanism.

EXPERIMENTAL PROCEDURES

Sample Preparation—CBD12, corresponding to residues 371–657 from canine NCX1 AD splice variant, was expressed as an eight residue His tag fusion in *Escherichia coli* BL21(DE3) cells (4). Uniform labeling with ^{15}N and ^{13}C was achieved by overexpression in M9 minimal medium supplemented with 5 g/liter of ^{13}C-labeled glucose and 1 g/liter of $^{15}NH_4Cl$ as the sole carbon and nitrogen sources, respectively. Random fractional deuteration was achieved by carrying out cell growth and protein expression in D_2O following standard procedures. *E. coli* cells were let grown in a minimal medium prepared in D_2O and supplemented with the adequate isotopes, 100 μg/liter ampicilin and 25 μg/liter thiamine-HCl. This inoculum was grown overnight, until the OD reached 0.9 at which point protein expression was induced by the addition of 0.5 mM of IPTG. Induction was performed for ~18 hs. Following cell lysis, protein purification was performed with a Ni-NTA column (Qiagen). The purified protein was desalted using a PD-10 desalting column (Amersham Biosciences), eluted with 20 mM Hepes pH 7.0, lyophilized and stored at −80 °C. NMR samples were prepared by dissolving CBD12 in 20 mM Hepes pH 7.0 containing 20 mM of β-mercaptoethanol and 10% D_2O. Apo samples also contained 15 mM EDTA and 100 mM NaCl. Alternatively, Ca^{2+}-bound samples contained 20 mM $CaCl_2$ and 80 mM NaCl. Buffer exchange and protein concentration were performed using an Amicon Ultra centrifugal device (Millipore) with 10 kDa cutoff.

NMR Spectroscopy—All NMR spectra were acquired at 306 K on a Bruker AVANCE III spectrometer, equipped with a TCI cryoprobe, operating at 800 MHz proton field. Backbone resonance assignments were obtained through the analysis of TROSY versions of HNCA, HNCOCA, HNCO, HNCACO, and HNCOCACB experiments, recorded on samples containing ~0.5 mM of $^{2}H/^{15}N/^{13}C$-labeled CBD12. Assignments for 78% (81%) of the backbone resonances of CBD12 in the Apo state (Ca^{2+}-bound state) could be obtained. Most of the cross-peaks in the center of the ^{15}N TROSY spectrum in the Apo state could not be assigned due to overlap. Unassigned residues are located in the disordered FG loop and in the segment between CBD1 and CBD2 (supplemental Fig. S1). In the Ca^{2+}-bound state, most of the unassigned residues correspond to cross-peaks that have very low amplitude or are completely absent in the ^{15}N TROSY spectrum (supplemental Fig. S1). RDCs were obtained from the analysis of ^{15}N HSQC and ^{15}N TROSY spectra acquired on samples of 445 μM $^{2}H,^{15}N$-labeled CBD12 aligned in 6% polyacrylamide gel, in the absence or presence of Ca^{2+}. Isotropic samples were measured under the same conditions. Peak positions in the ^{15}N TROSY and ^{15}N HSQC spectra were determined by fitting the cross-peaks to Gaussian functions using the Sparky software. Modeling of CBD12 based on the RDC data were performed by rotating each domain separately, so that their coordinate reference frames coincide with the frame of the respective alignment tensors. After rotation, CBD2 was translated relative to CBD1 such that the Cα atom of A502 of the two fragments superimposed. Because the RDCs are invariant under 180^0 rotations around the x, y, or z axis, this calculation generates 16 symmetric solutions (18), four of which are unique (19). The requirement that the correct solution obeys steric restrictions, allowed us to identify and discard physically unrealistic models. Longitudinal (R_1) and rotating-frame ($R_{1\rho}$) relaxation rates, and $\{^{1}H\}$-^{15}N steady-state nuclear Overhauser effects (NOE) were measured using standard ^{15}N relaxation methods (20, 21), recorded in pseudo-3D or interleaved fashion to minimize heating effects. Protein samples consisted of 330 μM (Apo) or 440 μM (Ca^{2+}-bound) $^{2}H,^{15}N$-labeled CBD12. During the $R_{1\rho}$ relaxation period a spin-lock field of $\gamma_N B_1/2\pi = 854$ Hz was applied. The experimental R_2 relaxation rates were obtained by correcting $R_{1\rho}$ for off-resonance effects using the relation $R_2 = R_{1\rho}/\sin^2(\theta) - R_1(\cos^2(\theta)/\sin^2(\theta))$, where $\tan(\theta) = \gamma_N B_1/2\pi\Delta\nu$ and $\Delta\nu$ is the resonance offset in Hz. The recycle delay was set to 3 s for all relaxation measurements. The NOE saturation period was 3 s. The R_1 and $R_{1\rho}$ relaxation times were determined from the fitting of the measured peak heights to an exponential decay function containing three parameters, namely the intensity at time 0, the decay rate, and a baseline offset. The uncertainty of the fitted parameters was determined by Monte Carlo simulations. The $R_{1\rho}$ relaxation rates were measured at two different ^{15}N carrier frequency offsets (113 and 123 ppm); the rate that is reported for a particular residue corresponds to the lower of the two χ^2 values. The translational diffusion coefficients were extracted by fitting translational diffusion decay curves as a function of gradient strength to a linear function as described in Ref. 22. The uncertainties in the translational diffusion coefficients were determined from the standard deviations of the diffusion coefficients measured at several specific peak positions along the ^{1}D DOSY spectrum of CBD12. All NMR spectra were processed with NMRPipe (23) and analyzed using the Analysis CCPNMR software (24). The backbone resonance assignments were deposited in the BMRB under the accession numbers 17721 and 17722.

RESULTS

Chemical Shift Analysis Reveals a Minimal Interaction Interface between CBD1 and CBD2—The two Ca^{2+}-binding domains are sequentially connected as part of the NCX intracellular loop. Analysis of the three-dimensional structures of isolated CBD1 and CBD2 indicates that a short segment comprising the six residues Asp-498 to Gly-503 connects the β-strand G of CBD1 to the β-strand A of CBD2 (Fig. 1 and supplemental Fig. S1). In this segment, amino acids Asp-498, Asp-499, and Asp-500 are part of the Ca^{2+}-binding sites Ca3 and Ca4 in CBD1 (5), while residues His-501, Ala-502, and Gly-

503 form the interdomain linker. Thus, the key questions are: how do the CBD1 and CBD2 domains interact with each other and how does Ca^{2+} binding to either one of the two domains modulate this interaction?

NMR backbone amide $^{1}H^{N}$ and ^{15}N chemical shifts are exquisitely sensitive to the local protein backbone conformation and the chemical environment of the nuclear spins. Because of this dependence, the two-dimensional ^{1}H-^{15}N HSQC spectrum, which correlates the resonances of directly attached ^{15}N and $^{1}H^{N}$ spins, serves as a fingerprint of the protein as each amino acid (except for Pro) gives rise to a backbone cross-peak signal. Perturbations of ^{1}H and ^{15}N chemical shifts due to ligand binding or protein-protein interactions are very useful to map interfaces of protein complexes or multidomain proteins. Here we use ^{1}H and ^{15}N NMR chemical shifts to investigate the interaction between the CBD1 and CBD2 domains in the absence and presence of Ca^{2+}.

As a first attempt to detect possible interactions between CBD1 and CBD2, we tested whether the isolated, *i.e.* noncovalently bonded, domains bind to each other in solution. NMR samples containing equal amounts of one domain ^{15}N-labeled and the other one unlabeled (so that it is invisible to NMR) were prepared in the absence and presence of 20 mM of $CaCl_2$. However, we did not observe any significant chemical shift changes in the ^{15}N HSQC spectrum of the ^{15}N-labeled domain upon the addition of the other (unlabeled) domain, indicating that the isolated CBDs do not bind to each other under these experimental conditions. This conclusion is consistent with other recent observations (16).

We then investigated how CBD1 and CBD2 interact with each other in the context of the larger CBD12 fragment. This construct corresponds to residues 371–657 of the NCX1-AD splice variant. Because of the large molecular mass of the CBD12 construct (32 kDa), we recorded ^{15}N-TROSY experiments instead of the ^{15}N-HSQC. Although the two experiments display the same type of spectral information, TROSY offers improved sensitivity and resolution for large molecular weight proteins at high magnetic fields (25). Visual inspection of the ^{15}N TROSY spectrum of CBD12 in the absence of Ca^{2+} shows minor differences in cross-peak positions with respect to the ^{15}N HSQC spectra of the individual domains (Fig. 2*A*). To quantify these spectral differences, we assigned the backbone resonances ($^{1}H^{N}$, ^{15}N, $^{13}C\alpha$, $^{13}C\beta$, and $^{13}C'$) of CBD12 in both the absence and presence of Ca^{2+} (supplemental Fig. S1). Quantitative comparison of ^{1}H and ^{15}N backbone chemical shifts with respect to the isolated domains in the Apo state confirms that the perturbations due to the presence of the linker are minor, *i.e.* smaller than 0.12 ppm (Fig. 3*A*). The largest changes are observed for Glu-E451 in the EF loop of CBD1, Ser-529, Ala-531, and Arg-532 in the BC loop and Met-631 and Gly-632 in the α-helix of the FG loop in CBD2 (Fig. 3*A*). These perturbations occur for residues that are spatially close to the

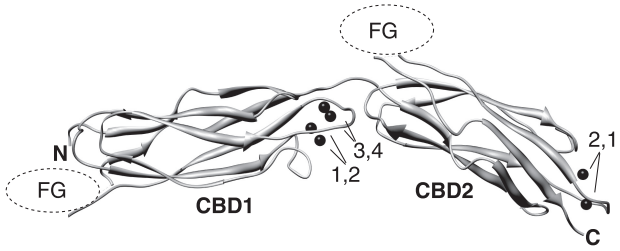

FIGURE 1. **Elongated arrangement of CBD1 and CBD2 in the tandem CBD12 construct.** The model was built by individual rotation and translation of the crystal structures of CBD1 (2DPK) and CBD2 (2QVM) according to the NMR residual dipolar coupling data obtained for the Apo state as described in the text. The two domains are superimposed at Ala-502. The Ca^{2+} ions observed in the original structures are indicated by their numbers and represented as *black spheres*. FG refers to the FG loop of either domain, which are highly flexible and are not shown.

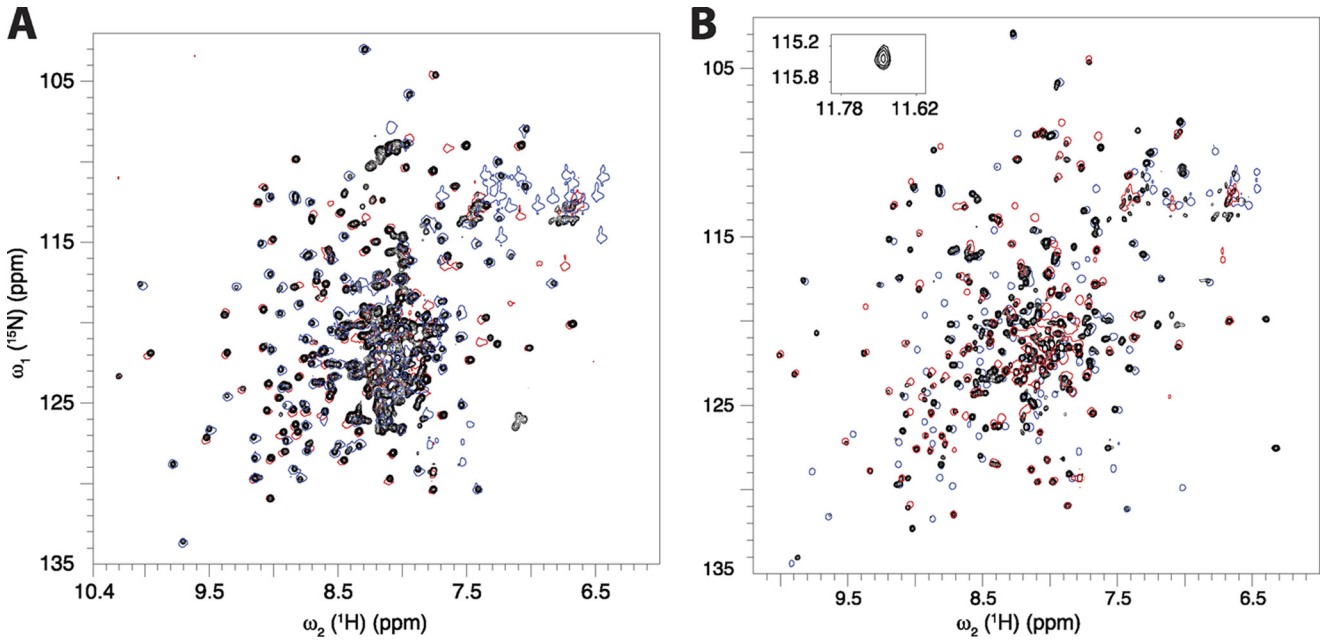

FIGURE 2. **^{15}N TROSY spectrum of the tandem CBD12 construct (*black*) in comparison with the ^{15}N HSQC spectra of the individual CBD1 (*blue*) and CBD2 (*red*) domains.** *A*, apo state; *B*, Ca^{2+}-bound state. For clarity, the spectra of the isolated domains are drawn using only one contour level. The cross-peak of Gly-503 in the Ca^{2+}-bound state is shown as an *inset*. The cross-peaks of the linker, which could not be assigned in the Apo state, are likely to fall into the congested central region. The two NMR samples contained 300 μM $^{2}H/^{15}N$ doubly-labeled CBD12.

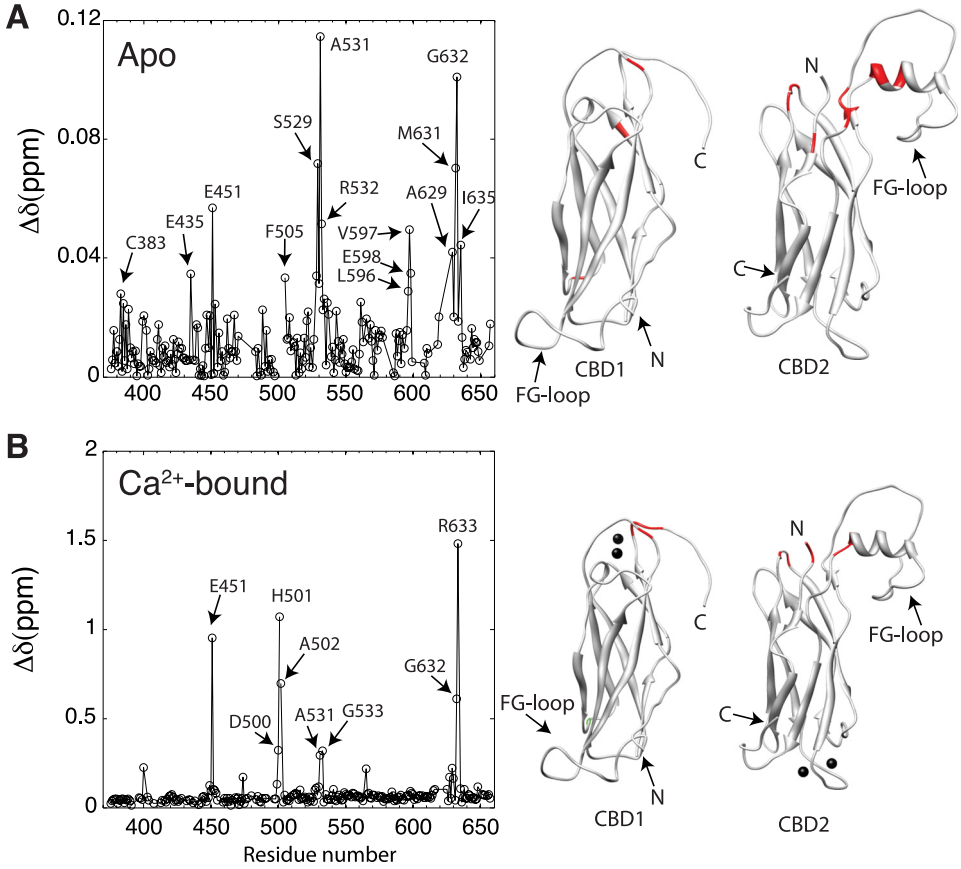

FIGURE 3. **Effect of the linkage of CBD1 and CBD2 on ^{15}N,^{1}H chemical shifts.** *A*, apo state, *B*, Ca^{2+}-bound state. The plots show weighted differences of ^{1}H and ^{15}N chemical shifts between CBD12 and the individual CBD1 and CBD2 domains as a function of the residue number. Amino acids showing differences larger than one standard deviation above the mean are indicated by *arrows* and colored in *red* in the three-dimensional structures of CBD1 (1FWS) and CBD2 (1FWU). The chemical shift difference was calculated according to: $\Delta\delta = \sqrt{(\delta^2_{HN} + 0.1\Delta\delta^2_N)}$.

interdomain linker in CBD12 (Fig. 3*A*), indicating the lack of a large interdomain interface. Moreover, the linker, which is relatively short, does not alter the three-dimensional structures of CBD1 and CBD2. Because of extensive spectral overlap (Fig. 2*A*) it was not possible to assign the resonances of segment 498–503 in the Apo state (supplemental Fig. S1).

In the Ca^{2+}-bound state, the chemical shift perturbations (CSP) in CBD1 and CBD2 because of the presence of the linker are much more significant, *i.e.* up to 1.5 ppm (Fig. 3*B*). A large chemical shift change is observed for Glu-451, which contacts Ca1, Ca2, and Ca3 in CBD1 via its side chain carboxyl moiety (5). Large chemical shift changes with respect to the individual domains are also observed in segment 498–503, including Asp-499 (CSP 0.1314 ppm) and Asp-500 (CSP 0.3201 ppm) that coordinate Ca3 and Ca4 in CBD1 via the side-chain carboxyl group (5), and the Glu-503 amide proton which is shifted to 11.69 ppm, in comparison with 9.89 ppm in CBD2 alone (Fig. 2*B*); the chemical shift changes stop at Ile-504, the first residue of the A β-strand in CBD2 (Fig. 3*B*). Similarly to the Apo state, residues Ala-531, Gly-533, Asp-565 in the BC and DE loops at the N-terminal side of CBD2, as well as Arg-627, Ala-629, Gly-632, and Arg-633 in the α-helix of the FG loop, show significant chemical shift perturbations due to the presence of the linker, pointing to their spatial proximity to CBD1. Thus, an important novel finding is that the two domains of CBD12 do not share a sizable interaction surface area when in their covalently linked form in CBD12. In both the Apo and the Ca^{2+}-bound states the interdomain interface between CBD1 and CBD2 is restricted to the EF Ca^{2+} binding loop in CBD1, the BC loop and the C-terminal end of the FG loop α-helix in CBD2. The absence of extensive chemical shift changes relative to the isolated domains indicates that the overall three-dimensional structures of the two domains are unaltered by their mutual presence.

Ca^{2+} Binding Is Sequential—It is well established that the isolated CBD1 binds Ca^{2+} tighter than CBD2 (4, 26), and displays slower Ca^{2+} off-rates (26). The different kinetic properties of isolated CBD1 and CBD2 are consistent with NMR observations, which demonstrate that Ca^{2+} binding occurs in different chemical exchange regimes, namely slow exchange in the case of CBD1 (not shown) and fast exchange for CBD2 (15). In the CBD12 construct, interdomain interactions modulate the Ca^{2+} dissociation rate at a specific binding site in the CBD1 domain, from which Ca^{2+} dissociates at a significantly slower off-rate of 0.4 s^{-1} (16).

To obtain insight into Ca^{2+} binding of CBD12 from a residue-level perspective, we performed a titration experiment in which changes in the ^{15}N TROSY spectra of CBD12 were monitored in response to the increase of Ca^{2+} concentration in a stepwise manner. Consistent with the behavior of the isolated domains (14, 15, 26), approximately four Ca^{2+} ions bind first to CBD1, and two Ca^{2+} ions bind to CBD2. Furthermore, Ca^{2+}

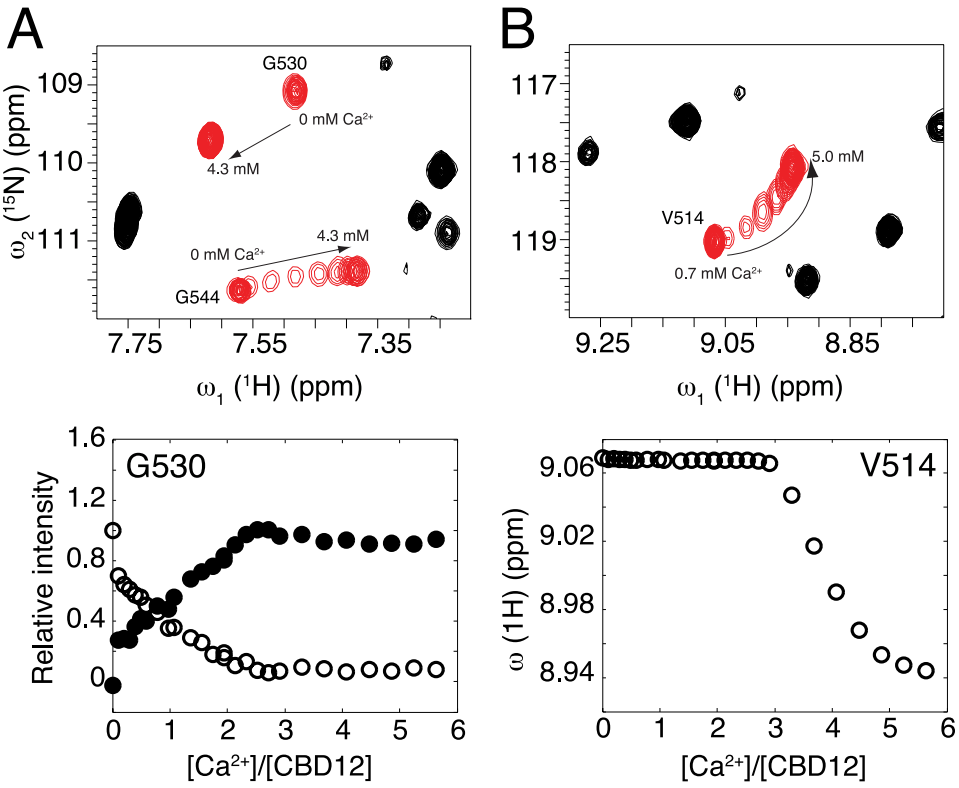

FIGURE 4. **Ca^{2+} titration of CBD12.** Selected regions of the ^{15}N TROSY spectra of CBD12 acquired in the presence of increasing Ca^{2+} concentrations. Specific residues that shift in slow or fast exchange upon Ca^{2+} binding are shown in *red* (*top*), and the variations in relative peak intensity or peak position as a function of [Ca^{2+}]:[CBD12] molar ratio are shown at the *bottom*. *Arrows* indicate the direction of cross-peak trajectories in the spectrum. In *A* CBD1 binds Ca^{2+} first, and Ca^{2+} binding influences the amino acids located at the N-terminal side of CBD2 such as Gly-530. The observation of two individual resonances for Gly-530, one for the bound and the other for the free species, is indicative of interconversion rates that are slow on the NMR chemical shift time scale (ms). In *B* CBD2 starts to bind Ca^{2+} only after the Ca^{2+}-binding sites of CBD1 have reached saturation. The cross-peak position of Val-514 follows a non-linear titration trajectory starting at the chemical shift position of the free state toward the chemical shift position of the bound state as the population of bound molecules increases. The observation of a single peak at the chemical shift corresponding to the population average of free and bound species is indicative of interconversion rates that are fast on the NMR time scale.

binding to CBD1 occurs in the form of a slow exchange equilibrium and in an all-or-none fashion (Fig. 4*A*). Binding of two Ca^{2+} ions to CBD2 only start to occur when the Ca^{2+}-binding sites in CBD1 reach saturation (Fig. 4*B*) with differentially Ca^{2+}-bound states being in fast exchange (Fig. 4*B*). This result shows that the binding of regulatory Ca^{2+} to the exchanger occurs in the CBD1 domain first, localizing unambiguously the binding sites for which K_d values were determined previously without spatial information by calorimetric titration measurements and binding curves of $^{45}Ca^{2+}$ (14, 16, 26).

It is worth noting that CBD2 residues close to the interdomain interface shift in slow exchange as Ca^{2+} binds to CBD1, but they do not react to the binding of Ca^{2+} to CBD2, which occurs at a long-range distance (Fig. 4*A*). NMR titration curves of Ca^{2+} binding to CBD2 could be adequately fitted to a stoichiometric model involving two independent binding sites. Estimates for the macroscopic dissociation constants (K_d) are 13.6 μM for the first binding event and 45.1 μM for the second one. These values are close to the K_d values derived for the isolated CBD2 from $^{45}Ca^{2+}$ equilibrium binding curves (5.3 and 22 μM) and NMR titration (16 and 24 μM) (15, 16). Interestingly, the cross-peaks of Val-514, Ile-520, Arg-547, and Gly-548, which are located at or near the Ca^{2+} binding loops in CBD2, do not follow a straight trajectory during titration, indicating the formation of an intermediate state in an anti-cooperative manner. These residues display analogous behavior in CBD2 alone (not shown). Negative cooperativity in Ca^{2+} binding with the formation of at least one intermediate state was also noted for the C2A domain of synaptotagmin I, and for the C2 domain of PKC-β (27, 28), and therefore may be a general characteristic of C2 domains.

CBD12 Assumes on Average an Elongated Shape in the Absence and Presence of Ca^{2+}—Neither an x-ray crystal structure nor an NMR structure of CBD12 has been reported to date. To get more detailed structural information about CBD12 we measured one-bond backbone ^{1}H-^{15}N residual dipolar couplings (RDCs) of CBD12 partially aligned in compressed polyacrylamide gel (29, 30). NMR ^{1}H-^{15}N RDCs contain information about the average orientation of ^{1}H-^{15}N bond vectors with respect to the external magnetic field (31), which can be used to characterize the orientations of individual domains of a multidomain protein relative to a common alignment tensor (31, 32). A set of 39 dipolar couplings was obtained for the Apo state. Because of the much larger line widths, only 16 dipolar couplings could be measured in a quantitative manner for the Ca^{2+}-bound state.

The alignment tensor of each individual domain was calculated by a linear least-squares fit of the ^{1}H-^{15}N RDCs to the crystal structures of CBD1 (2DPK) and CBD2 (2QVM) using singular value decomposition (19). The agreement between

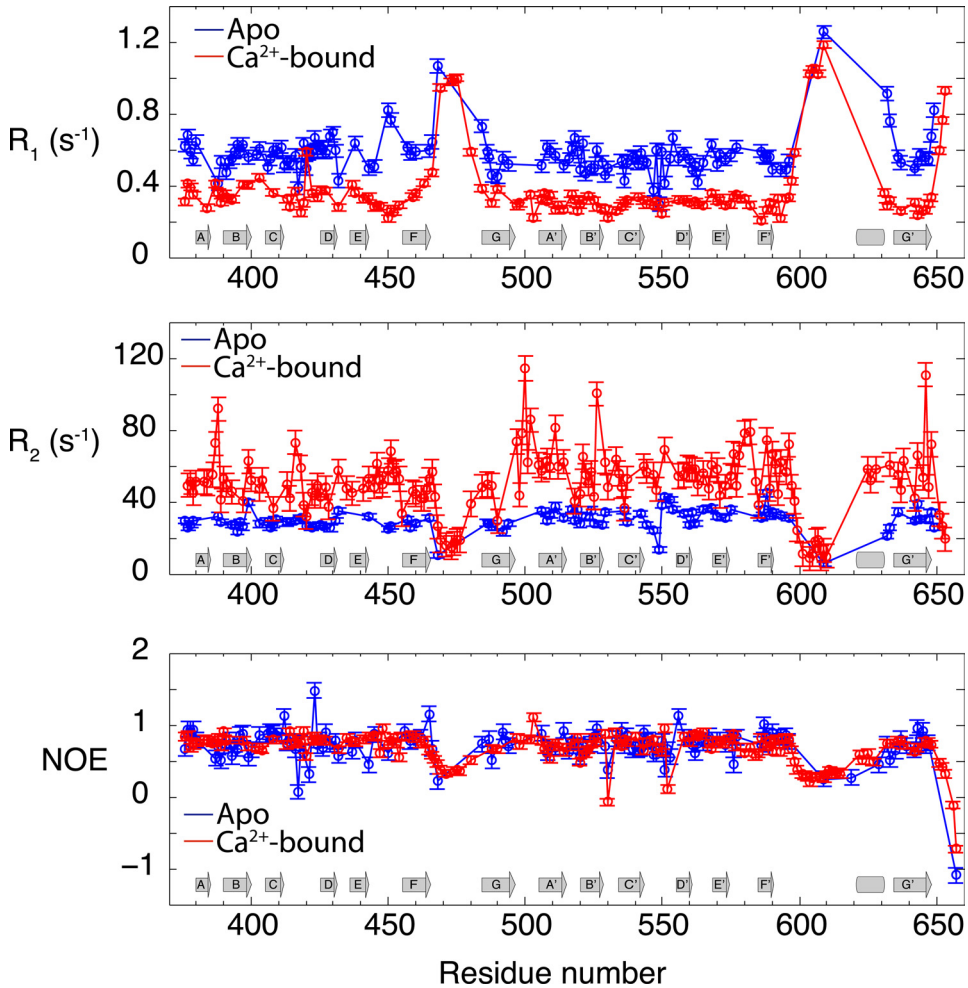

FIGURE 5. **Backbone ^{15}N R_1 and R_2 relaxation rates and heteronuclear {^1H}-^{15}N NOE in the Apo (*blue*) and Ca^{2+}-bound (*red*) states of CBD12.** The approximate positions of the secondary structure elements of CBD12 are shown at the *bottom*, with β-strands represented by *arrows* and the α-helix by a *cylinder*. Interruptions of the β-strands due to the β-bulge (strand A) and *cis*-Pro (strand G) are not represented. The protein concentrations used in these studies were 330 and 441 μM of $^2H/^{15}N$ doubly labeled CBD12 in the Apo and Ca^{2+}-bound states, respectively.

experimental and RDCs back-calculated based on the crystal structures is visualized in supplemental Fig. S2. Models of CBD12 were generated as described under "Experimental Procedures." Fig. 1 shows the allowed solution for the Apo state, which adopts an elongated shape with an extended, nearly 180° angle between the orientations of CBD1 and CBD2 (Fig. 1). An analogous analysis for the Ca^{2+}-bound state indicates that it adopts a similarly elongated shape. However, the smaller number of dipolar couplings measurable for this state limits the accuracy of the alignment tensors and of the associated interdomain angle.

The predominance of elongated, nearly linear average overall structures in the absence and presence of Ca^{2+} is in good agreement with the interdomain interface mapped by chemical shift perturbations, as shown in Fig. 3. In the final orientation, the α-helix and one loop of the CBD2 domain are oriented toward the EF Ca^{2+}-binding loop of CBD1, close to the Ca3 and Ca4 binding sites (Fig. 1). The prevalence of a relatively elongated structure is also consistent with the short length of the linker that connects CBD1 to CBD2, which hinders a side-by-side configuration of these 2 large domains. One must note, however, that the accuracy of the orientation between CBD1 and CBD2 along the axes perpendicular to the β-sandwich core is limited due to the intrinsic symmetry of the problem, and due to the fact that RDCs could only be obtained in a single alignment medium.

Ca^{2+} Binding Rigidifies Linker Residues 501–503 Increasing the Dynamic Coupling between CBD1 and CBD2—NMR spin relaxation provides atomic detail information on ns-ps dynamics of ^{15}N-^1H bond vectors along the protein backbone. Moreover, ^{15}N relaxation data are highly informative about the overall rotational diffusion (tumbling) and its anisotropy. Therefore, to characterize the interdomain flexibility and internal backbone dynamics of CBD12 in the absence and presence of Ca^{2+}, we measured backbone ^{15}N longitudinal (R_1) and transverse (R_2) relaxation rates and the {^1H}-^{15}N heteronuclear steady state nuclear Overhauser effect (NOE) of CBD12 in the Apo and Ca^{2+}-bound states. Fig. 5 shows plots of R_2, R_1, and NOE as a function of the amino acid sequence for CBD12 in the Apo and Ca^{2+}-bound states. The overall pattern of the ^{15}N NMR relaxation rates and the NOE are similar to the patterns previously observed for the isolated domains, characteristic of rigid β-sandwich cores and mobile FG loops (13, 15). The mean R_1, R_2, and NOE along the β-sandwich core are 0.59 s^{-1}, 27.90

TABLE 1

Overall rotational correlation times (ns) of the CBD1 and CBD2 domains isolated and linked in CBD12

The anisotropic overall rotational correlation times displayed for the isolated CBD domains were obtained from Johnson *et al.* and Breukels and Vuister (13, 15). The isotropic rotational correlation times of CBD1 and CBD2 in the CBD12 construct are the mean local correlation times calculated using the software r2r1_tm provided by Dr. Arthur G. Palmer III, and using as input the R_2/R_1 ratios of transverse and longitudinal ^{15}N relaxation rates measured for CBD12 in the Apo and Ca^{2+}-bound states.

	CBD1	CBD2
CBD12 Apo	16.92 ± 1.73	18.69 ± 1.38
CBD12 Ca^{2+}-bound	30.18 ± 4.55	33.33 ± 3.82
Isolated domains Apo	11.03 ± 0.02	11.4 ± 2.3

s^{-1}, and 0.75, respectively, for CBD1, and 0.55 s^{-1}, 32.46 s^{-1}, and 0.74 for CBD2, in the Apo state. It is noteworthy that Ca^{2+} binding induces a large change in the relaxation rates throughout CBD12 (Fig. 5). In the Ca^{2+}-bound state, the mean R_1, R_2, and NOE values for CBD1 along the β-sandwich are 0.34 s^{-1}, 51.26 s^{-1}, and 0.76, respectively, and 0.30 s^{-1}, 56.72 s^{-1}, and 0.74, respectively, for CBD2.

The overall correlation time (τ_c) for Brownian rotational diffusion estimated from the ^{15}N relaxation data along the β-sandwich core of Apo CBD12 is 16.92 ± 1.73 ns for CBD1, and 18.69 ± 1.38 ns for CBD2. These values are 35–39% larger than the overall anisotropic rotational tumbling time of the isolated CBD domains under similar sample conditions (Table 1) (13, 15). The larger τ_c observed in the case of CBD12 is consistent with two domains tethered by a short flexible linker. They neither tumble completely independently from each other nor together as a rigid body (33). By contrast, in the Ca^{2+}-bound state the overall τ_c increases to 30.18 ± 4.55 ns for CBD1 and 33.33 ± 3.82 ns for CBD2 (Table 1), indicating much slower reorientational motions than in the Apo state. We note that overall changes in the NOE between Apo and Ca^{2+} bound states are not expected (Fig. 5), because the NOE depends predominantly on higher frequency motions, which are unrelated to the overall tumbling behavior.

Importantly, dimerization (or higher order oligomerization) is not the cause for the reduced tumbling rate observed in the Ca^{2+}-bound state. The translational diffusion coefficient of CBD12 measured by diffusion-ordered NMR spectroscopy (DOSY) is ~7.4×10^{-11} m^2 s^{-1} (supplemental Table SI). This value is consistent with a globular 33-kDa protein. The Ca^{2+}-bound form has a systematic tendency to translationally diffuse faster than the Apo form. However, this difference is close to the standard deviation of the fitted diffusion coefficient, which is ~5%. In addition, van Holde-Weischet analysis of sedimentation velocity analytical ultracentrifugation (AUC) experiments indicate that samples of CBD12 at concentrations similar to those used for the NMR experiments (300 μM) contain mostly single species characterized by a sedimentation coefficient of ~2.6 S (supplemental Fig. S3). This value is consistent with hydrodynamic calculations made using either HYDRO-PRO (34) or SOMO (35) software. Values of 3.89 S and 6.01 S would be expected for a dimer, equivalent to a 64 kDa protein with a prolate or spherical shape, respectively. While the Apo state of CBD12 starts to aggregate after 3 days in the spectrometer, the addition of Ca^{2+} stabilizes the protein as a whole, preventing aggregation. Structural stabilization due to Ca^{2+} binding was also observed for other C2 domains (28).

The individual τ_c values observed for the two domains in the Ca^{2+}-bound state, 30.18 ns and 33.33 ns for CBD1 and CBD2, respectively, are almost twice the size of the ones of the Apo state and close to each other (Table 1). This suggests that in the Ca^{2+}-bound state the two domains are firmly attached to each other. By contrast, in the Apo state the two domains are linked flexibly. This is further corroborated by the RDC data: the dynamic range of the RDCs as measured by their standard deviation drops from 18.2 Hz for the Ca^{2+}-bound state to 10.8 Hz in the Apo state under identical alignment conditions. The wide distribution of interdomain orientations probed in the Apo state leads to additional averaging of the dipolar couplings manifested in the reduced standard deviation as compared with the Ca^{2+}-bound state.

The Linker Dynamics—The slower overall rotational tumbling of CBD12 in the Ca^{2+}-bound state relative to the Apo state must stem from the restriction of the linker motions on the nanosecond timescale due to Ca^{2+} binding to CBD1. Because of spectral overlap and lack of resonance assignments, it was not possible to directly study the dynamics of the linker amino acids His-501—Gly-503 in the Apo state. However, the relatively fast overall rotational tumbling time of CBD12 in the Apo state provides evidence for flexibility of the linker. In the presence of Ca^{2+}, the mean R_1, R_2, and NOE values along the linker formed by residues H501-G503 (0.28 ± 0.03 s^{-1}, 73.84 ± 14.63 s^{-1}, and 0.90 ± 0.12 s^{-1}, respectively) are compatible with a segment that is relatively rigid on the nanosecond timescale (Fig. 5). The involvement of Asp-498, Asp-499, and Asp-500, with the coordination of Ca3 and Ca4 in CBD1, makes Ca^{2+} binding the lead mechanism for the restriction of interdomain mobility (Fig. 1). Altered ^{15}N R_1 and R_2 relaxation rates can be detected under conditions where only the CBD1 Ca^{2+}-binding sites are occupied. As shown in supplemental Fig. S4, R_1 and R_2 relaxation rates obtained in the presence of a 3-fold excess of Ca^{2+}, where Ca^{2+} is mostly bound to CBD1, coincide well with those observed in the Ca^{2+}-saturated state where the Ca^{2+}-binding sites of CBD2 are also occupied. Thus, Ca^{2+} binding to CBD1 alone is responsible for the restriction of the linker flexibility.

In summary, the ^{15}N relaxation analysis of CBD12 in the Apo state is consistent with the two domains coupled only weakly to each other. In this state, CBD1 and CBD2 sample a wide range of relative arrangements on the nanosecond time scale, which include the elongated conformation of the Ca^{2+}-bound state, but mostly comprises significantly non-linear interdomain orientations. Specific binding of Ca^{2+} to CBD1 dramatically strengthens the dynamic coupling with CBD2 and thereby reduces the overall rotational tumbling rate in a manner that is consistent with the predominant presence of the elongated orientations.

DISCUSSION

Early studies showed that treatment with chymotrypsin converts the NCX into a fully active and deregulated exchanger (10). This finding demonstrated that the intracellular loop plays a key role in ionic regulation. This conclusion is also valid for

CALX1.1, a NCX from *Drosophila melanogaster* that exhibits the opposite effect upon the binding of regulatory Ca^{2+}, *i.e.* inhibition instead of activation (36). The NCX intracellular loop contains two Ca^{2+} sensors, CBD1 and CBD2 with different thermodynamic and kinetic Ca^{2+} binding properties (16, 26). Despite efforts to characterize the structure and dynamics of the isolated CBD1 and CBD2 by NMR and x-ray crystallography, mechanisms of NCX ionic regulation are still unknown at an atomic level.

As pointed out by Nicoll *et al.* (5), Ca^{2+} binding to CBD1 involves additional acidic residues Asp-498, Asp-499, and Asp-500, which follow β-strand G of CBD1. These residues, which have no counterpart in the C2 domains of synaptotagmin-1 and in PKC, participate in the coordination sphere of Ca3 and Ca4 in CBD1 (5, 9). In this work we showed unambiguously that Ca^{2+}-binding restricts the flexibility of the linker between CBD1 and CBD2 to the extent that CBD12 assumes a predominantly elongated conformation (Fig. 1). These observations explain recent measurements of FRET by John and co-workers (2011) (17), which indicated that Ca^{2+} binding to CBD1 increases the distance between the N- and C termini of CBD12 (17). Because FRET monitors $\sim 1/r^6$ distance averaging, the contributions of the non-linear interdomain arrangements probed in the Apo state lead to a reduced effective distance between the N- and C termini compared with the elongated rigidified Ca^{2+}-bound form. Although a study by SAXS has suggested that the binding of Ca^{2+} to CBD12 induces changes in the interdomain orientation (14), a comparison between our findings and previous SAXS measurements is not straightforward because in the case of the Apo state one must account for its heterogeneous dynamic ensemble character, which is quantitatively different from the rigidified Ca^{2+}-bound state.

Slow conformational changes occur in the cytoplasmic loop of the full-length NCX and in CBD12 upon Ca^{2+} removal, as previously detected by FRET (17). These motions occur on a second time scale (17), and may be associated with the slow dissociation of Ca^{2+} from the CBD1 domain (16). Although from our NMR study we do not have fully time-resolved information about slow interdomain dynamics in CBD12, the larger alignment tensor obtained from ^{1}H-^{15}N RDCs in the Ca^{2+}-bound state gives direct evidence that the linker between CBD1 and CBD2 maintains its rigidity at least up to the millisecond time scale. These findings are consistent with the ^{15}N relaxation results in as far as reduced mobility on the faster time scales is a prerequisite for rigidity on the slower time scales.

These conclusions reveal interesting parallels to the interdomain dynamics of adjacent C2 domains, which are ubiquitous Ca^{2+}-binding motifs found in different protein families (37–40). Cadherins are a family of cell surface proteins involved in Ca^{2+}-dependent cell adhesion (38). In analogy with CBD12, the binding of Ca^{2+} to a two-ectodomain cadherin construct restricts the linker motions substantially (38, 41). However, the Ca^{2+}-binding modes of cadherins and CBD12 are distinct. The binding of Ca^{2+} by the two-ectodomain cadherin construct involves direct contacts with residues in the linker region, whereas the binding of Ca^{2+} to sites Ca3 and Ca4 in CBD1 involves contacts with residues 498–500 that directly precede linker residues 501–503.

Several lines of evidence are consistent with the notion that the linker between CBD1 and CBD2 plays an important role in the mechanism of Ca^{2+} regulation. Specifically, electrophysiological studies of wild type and mutant exchangers showed that Ca^{2+} binding at sites Ca3 and Ca4 (but not Ca1 and Ca2) in CBD1 is essential for Ca^{2+} regulation (6, 11, 12, 42). Substitution G503P in the linker greatly affects the sensitivity of both NCX1.1 and CALX1.1 to intracellular Ca^{2+} (5, 36, 42), although this amino acid is not part of the Ca^{2+}-binding site. The insertion of seven alanines between His-501 and Ala-502 in the linker decreases the apparent affinity of the exchanger for regulatory Ca^{2+} and increases the Ca^{2+} off-rates of a specific Ca^{2+}-binding site from CBD1 in the CBD12 construct (16, 43). And finally, a study of FRET demonstrated that Ca^{2+} binding to CBD1 induces motions in the intracellular loop of full-length functional exchangers (17). These results indicate that Ca^{2+} binding to the Ca3 and Ca4 sites acts as a trigger event for NCX activation. The results of the present study clarify the functional role of Ca^{2+} binding by demonstrating that it substantially reduces the flexibility of CBD12 locking it into the elongated shape. It is postulated that changes in CBD12 interdomain flexibility by the binding of Ca^{2+} to CBD1 are part of the mechanism of allosteric Ca^{2+} regulation.

Acknowledgments—We thank Dr. M. Hilge for providing the plasmid coding for CBD12, and Dr. C. Mumdoma of the Physical Biochemistry Facility at FSU for AUC experimental design and data analysis.

REFERENCES

1. Lytton, J. (2007) *Biochem. J.* **406,** 365–382
2. Reeves, J. P., and Condrescu, M. (2008) *Channels* **2,** 322–328
3. Philipson, K. D., and Nicoll, D. A. (2000) *Annu. Rev. Physiol.* **62,** 111–133
4. Hilge, M., Aelen, J., and Vuister, G. W. (2006) *Mol. Cell* **22,** 15–25
5. Nicoll, D. A., Sawaya, M. R., Kwon, S., Cascio, D., Philipson, K. D., and Abramson, J. (2006) *J. Biol. Chem.* **281,** 21577–21581
6. Besserer, G. M., Ottolia, M., Nicoll, D. A., Chaptal, V., Cascio, D., Philipson, K. D., and Abramson, J. (2007) *Proc. Natl. Acad. Sci. U.S.A.* **104,** 18467–18472
7. Wu, M., Wang, M., Nix, J., Hryshko, L. V., and Zheng, L. (2009) *J. Mol. Biol.* **387,** 104–112
8. Wu, M., Le, H. D., Wang, M., Yurkov, V., Omelchenko, A., Hnatowich, M., Nix, J., Hryshko, L. V., and Zheng, L. (2010) *J. Biol. Chem.* **285,** 2554–2561
9. Rizo, J., and Südhof, T. C. (1998) *J. Biol. Chem.* **273,** 15879–15882
10. Hilgemann, D. W. (1990) *Nature* **344,** 242–245
11. Ottolia, M., Nicoll, D. A., and Philipson, K. D. (2009) *J. Biol. Chem.* **284,** 32735–32741
12. Chaptal, V., Ottolia, M., Mercado-Besserer, G., Nicoll, D. A., Philipson, K. D., and Abramson, J. (2009) *J. Biol. Chem.* **284,** 14688–14692
13. Johnson, E., Bruschweiler-Li, L., Showalter, S. A., Vuister, G. W., Zhang, F., and Brüschweiler, R. (2008) *J. Mol. Biol.* **377,** 945–955
14. Hilge, M., Aelen, J., Foarce, A., Perrakis, A., and Vuister, G. W. (2009) *Proc. Natl. Acad. Sci. U.S.A.* **106,** 14333–14338
15. Breukels, V., and Vuister, G. W. (2010) *Proteins* **78,** 1813–1824
16. Giladi, M., Boyman, L., Mikhasenko, H., Hiller, R., and Khananshvili, D. (2010) *J. Biol. Chem.* **285,** 28117–28125
17. John, S. A., Ribalet, B., Weiss, J. N., Philipson, K. D., and Ottolia, M. (2011) *Proc. Natl. Acad. Sci. U.S.A.* **108,** 1699–1704
18. Hus, J. C., Salmon, L., Bouvignies, G., Lotze, J., Blackledge, M., and Brüschweiler, R. (2008) *J. Am. Chem. Soc.* **130,** 15927–15937
19. Losonczi, J. A., Andrec, M., Fischer, M. W., and Prestegard, J. H. (1999) *J. Magn. Reson.* **138,** 334–342
20. Brutscher, B., Brüschweiler, R., and Ernst, R. R. (1997) *Biochemistry* **36,**

13043–13053
21. Massi, F., Johnson, E., Wang, C., Rance, M., and Palmer, A. G., 3rd. (2004) *J. Am. Chem. Soc.* **126,** 2247–2256
22. Chou, J. J., Baber, J. L., and Bax, A. (2004) *J. Biomol. NMR* **29,** 299–308
23. Delaglio, F., Grzesiek, S., Vuister, G. W., Zhu, G., Pfeifer, J., and Bax, A. (1995) *J. Biomol. NMR* **6,** 277–293
24. Vranken, W. F., Boucher, W., Stevens, T. J., Fogh, R. H., Pajon, A., Llinas, M., Ulrich, E. L., Markley, J. L., Ionides, J., and Laue, E. D. (2005) *Proteins* **59,** 687–696
25. Pervushin, K., Riek, R., Wider, G., and Wüthrich, K. (1997) *Proc. Natl. Acad. Sci. U.S.A.* **94,** 12366–12371
26. Boyman, L., Mikhasenko, H., Hiller, R., and Khananshvili, D. (2009) *J. Biol. Chem.* **284,** 6185–6193
27. Ubach, J., Zhang, X., Shao, X., Südhof, T. C., and Rizo, J. (1998) *EMBO J.* **17,** 3921–3930
28. Shao, X., Davletov, B. A., Sutton, R. B., Südhof, T. C., and Rizo, J. (1996) *Science* **273,** 248–251
29. Tycko, R., Blanco, F. J., and Ishii, Y. (2000) *J. Am. Chem. Soc.* **122,** 9340–9341
30. Sass, H. J., Musco, G., Stahl, S. J., Wingfield, P. T., and Grzesiek, S. (2000) *J. Biomol. NMR* **18,** 303–309
31. Blackledge, M. (2005) *Prog. Nucl. Mag. Res. Sp.* **46,** 23–61
32. Fushman, D., Varadan, R., Assfalg, M., and Walker, O. (2004) *Prog. Nucl. Mag. Res. Sp.* **44,** 189–214
33. Walsh, J. D., Meier, K., Ishima, R., and Gronenborn, A. M. (2010) *Biophys. J.* **99,** 2636–2646
34. García, de la Torre, J. G., Huertas, M. L., and Carrasco, B. (2000) *Biophys. J.* **78,** 719–730
35. Brookes, E., Demeler, B., and Rocco, M. (2010) *Macromol. Biosci.* **10,** 746–753
36. Dyck, C., Maxwell, K., Buchko, J., Trac, M., Omelchenko, A., Hnatowich, M., and Hryshko, L. V. (1998) *J. Biol. Chem.* **273,** 12981–12987
37. Min, S. W., Chang, W. P., and Südhof, T. C. (2007) *Proc. Natl. Acad. Sci. USA* **104,** 3823–3828
38. Shapiro, L., and Weis, W. I. (2009) *Cold Spring Harb. Perspect. Biol.* **1,** a003053
39. Bansal, D., and Campbell, K. P. (2004) *Trends Cell Biol.* **14,** 206–213
40. Südhof, T. C. (2002) *J. Biol. Chem.* **277,** 7629–7632
41. Häussinger, D., Ahrens, T., Sass, H. J., Pertz, O., Engel, J., and Grzesiek, S. (2002) *J. Mol. Biol.* **324,** 823–839
42. Matsuoka, S., Nicoll, D. A., Hryshko, L. V., Levitsky, D. O., Weiss, J. N., and Philipson, K. D. (1995) *J. Gen. Physiol.* **105,** 403–420
43. Ottolia, M., Nicoll, D. A., John, S., and Philipson, K. D. (2010) *Channels* **4,** 159–162